Uncertainty Quantification for Microstructure-Sensitive Fatigue Nucleation and Application to Titanium Alloy, Ti6242

Xiaoyu Zhang[†] , Yang Liu[‡] , and Caglar Oskay[†*]

[†] Department of Civil and Environmental Engineering
Department of Mechanical Engineering
Vanderbilt University
Nashville, TN 37212

[‡] Department of Materials
Imperial College London
London SW7 2AZ, United Kingdom

Abstract

Microstructure of polycrystalline materials has profound effects on fatigue crack initiation, and the inherent randomness in the material microstructure results in significant variability in fatigue life. This study investigates the effect of microstructural features on fatigue nucleation life of a polycrystalline material using an uncertainty quantification framework. Statistical volume elements (SVE) are constructed, where features are described as probability distributions and sampled using the Monte Carlo method. The concept of SVE serves as the tool for capturing the variability of microstructural features and consequent uncertainty in fatigue behavior. The response of each SVE under fatigue loading is predicted by the sparse dislocation density informed eigenstrain based reduced order homogenization model with high computational efficiency, and is further linked to the fatigue nucleation life through a fatigue indicator parameter (FIP). The aggregated FIP and its evolution are captured using a probabilistic description, and evolve as a function of time. The probability of fatigue nucleation is measured as the probability that the predicted FIP exceeds the local critical value which represents the ability of material to resist the fatigue load. The proposed framework is implemented and validated using the fatigue response of titanium alloy, Ti-6Al-2Sn-4Zr-2Mo (Ti-6242).

*Corresponding author address: VU Station B#351831, 2301 Vanderbilt Place, Nashville, TN 37235. Email: caglar.oskay@vanderbilt.edu

Keywords: Titanium alloy, Lamellar structure, Fatigue nucleation, Reduced order model, Uncertainty quantification.

1 Introduction

Quantitative evaluation of fatigue failure is an important factor for material and structural design of aircraft components that bear cyclic loads. Fatigue failure process consists of microcrack nucleation and short microstructure-sensitive crack growth (collectively referred to as fatigue initiation), long crack growth and final rupture. Experimental observations show that high cycle fatigue failure of polycrystalline materials could be dominated (up to 80-90% of life [35]) by crack initiation which, in turn, is significantly influenced by material microstructural features. The microstructures exhibit significantly varying features depending on processing conditions, and this inherent randomness results in significant uncertainty in fatigue life [6, 34, 41, 68]. In the current study, we propose an uncertainty quantification framework to quantify the effect of microstructure on fatigue nucleation life from a probabilistic point of view.

Fatigue failure of polycrystalline materials is shown to be significantly affected by material microstructure in both experimental and modeling investigations [14, 20, 46]. A large body of experimental work established aspects of the relationships between the fatigue crack formation and microstructural attributes (e.g., grain size [48], crystallographic orientation [48], grain interactions [1, 66], inclusion-matrix interaction [29], twin boundaries [11], surface topology/roughness [27], etc [44]) using imaging and characterization techniques such as electron backscatter diffraction, scanning electron microscopy, digital image correlation and others. The influence of microstructure attributes on the fatigue response of the polycrystalline materials has also been investigated numerically using the crystal plasticity finite element (CPFE) method [12, 13, 18, 46, 69, 72, 74, 53]. For instance the influence of macrozones or microtextured regions results in significant lifetime reduction under dwell fatigue, which are widely observed in α and $\alpha + \beta$ titanium alloy. The macrozone in Ti-6Al-4V, which has aspect ratio larger than 4 and basal poles within 15° of remote loading direction, leads to much higher stress redistribution [40]. Microstructural heterogeneity within neighboring α/β phases with specific orientation relationship plays a significant role in higher local creep resistance in basketweave structure compared to colony or Widmanstatten structure in $\alpha + \beta$ titanium alloys [68, 81].

Several sources of uncertainty contribute to the variability in fatigue initiation and consequently total fatigue lifetimes. These include the morphological features in the material microstructure [34], residual stress [28], experimental conditions associated with the loading, boundary conditions and testing environment [9], measurement techniques, among others. Probabilistic prediction of fatigue initiation based on computational modeling and simulation

includes additional sources of uncertainty including digitized representation of microstructure, model parameters, model form, and the fatigue indicator parameter (FIP) used to assess initiation.

A number of recent studies focused on incorporation of statistics and uncertainty into computational fatigue initiation prediction in polycrystalline materials. About a decade earlier, McDowell and coworkers proposed a microstructure analysis based probabilistic prediction paradigm that forms the foundation for several studies [51, 55, 56, 6]. The primary means to quantifying uncertainty is the aggregation of spatial distributions of FIPs obtained from a collection of CPFE simulations on Statistical Volume Elements (SVEs). Compared with the representative volume element (RVE), SVE concept allows statistical variability of the response from one realization to another since the size of an SVE is taken to be much smaller than an RVE. Considering an ergodic process, the ensemble response of SVEs captures the RVE response. The FIP computations are often performed as a post-processing step, where volume averaged FIPs over grains [40, 12] or sub-grain domains [26] provide the statistical data. Przybyla and McDowell [55, 56] connected microstructure attributes with certain extreme value fatigue response parameters to study the driving force of fatigue nucleation in Ni-based superalloy IN100 [55] and Ti-6Al-4V microstructures [56]. An important complicating factor in this regard is the very high computational cost of performing simulations over a sufficiently large SVE ensemble, that may be on the order of thousands or more [70]. This cost could be reduced by replacing CPFE simulations with microstructurally-informed homogenized constitutive models [34, 52], reduced-order microstructure models [78, 79], or machine learning models [10, 71], by establishing scalable and efficient CPFE solvers [73], or by judiciously limiting uncertainty analysis to a subset of geometric features obtained based on sensitivity analysis [80].

In addition to the uncertainty induced by microstructure heterogeneity, numerical discretizations and the constitutive models used to idealize unresolved subscale behavior also introduce uncertainty and error into initiation predictions. Yeratapally et al. [75] focused on the effect of model parameter uncertainty on the variability of fatigue initiation predictions. The number of parameters contributing to initiation variability is reduced by global sensitivity analysis (also employed in [80, 81]). Local parametric sensitivity analyses also provide information on critical parameters that affect fatigue initiation [71]. Anahid and Ghosh [2] developed a probabilistic crack nucleation model which links time for macroscopic crack nucleation to the macroscopic stress state and microstructural characteristic parameters. Kotha et al. [34] quantified model form uncertainty for a parametrically homogenized constitutive model and took the approach of SVE ensemble simulations to track FIP variability.

The aforementioned investigations (e.g., [5, 7]) have primarily focused on characterization of uncertainty in fatigue initiation parameters and their extreme value distributions since

fatigue is expected to initiate at regions of high FIP. We refer to this as "uncertainty in fatigue forces" loosely indicating that uncertainty in the microstructure is propagated to the response fields such as stress, strain, plastic strain, dislocation density or a combination thereof. In this study, borrowing from reliability analysis, we posit the existence of "uncertainty in fatigue resistance" and assess microstructure sensitive fatigue failure using a risk-based approach. Fatigue resistance refers to an inherently stochastic property that quantifies the ability of the material to sustain the aforementioned fatigue forces. By this approach, the probability of fatigue failure is computed using both the uncertainties in microstructural fatigue forces and resistances.

In the current study, we devised an uncertainty quantification framework to elucidate the linkage between microstructure and fatigue nucleation life, and exercised this framework to study fatigue nucleation in titanium alloy, Ti-6Al-2Sn-4Zr-2Mo (Ti-6242). Fatigue nucleation is modeled using the concept of FIP. FIP distribution over an SVE is computed using a dislocation density informed eigenstrain based reduced order homogenization Model (DD-EHM) [40] combined with the Sparse EHM formulation [79]. DD-EHM is a reduced order microstructure modeling approach that computes microstructure response at a fraction of the cost of a CPFE simulation. The SVEs are generated based on the probabilistic distributions of features, and the responses of these SVEs under cyclic loading are assembled to obtain the FIP distributions as a function of load cycles. The distribution of fatigue strength, i.e. the *critical* FIP distribution is taken as a material property, which is identified using experimental data. The probability of failure as a function of load cycles is then computed using the calibrated fatigue strength distribution and the predicted FIP distribution. Probability of fatigue nucleation for Ti-6242 are predicted at different stress levels as a validation of the proposed framework.

The remainder of this manuscript is organized as follows: Section 2 describes the proposed uncertainty quantification framework, including the parametric and probabilistic description of material microstructure, multiscale simulations and the probability of fatigue nucleation. Section 3 introduces the microstructure attributes of Ti-6242. Section 4 describes the DD-EHM formulation, the constitutive model employed in the forward simulations of the fatigue response, and the employed FIP. Section 5 discusses the uncertainties of microstructural attributes considered in this study. Detailed investigation and analysis for the relationship between microstructure and fatigue behavior are also presented in this section. Section 6 includes the summary and conclusions.

2 Overview of the Uncertainty Quantification Framework

The uncertainty quantification (UQ) framework used in this study is based on the idea that fatigue damage evolution at the scale of the material microstructure can be characterized by a fatigue indicator parameter, and that the probability of fatigue nucleation in the material microstructure is determined as the probability that the FIP exceeds a critical value after a prescribed number of load cycles. The probability of fatigue nucleation is therefore dictated by two distributions: (1) the spatial distribution of the FIP induced by microstructure heterogeneity under the applied loadings, which evolves as a function of load cycles; and (2) a random variable referred to as the *critical* FIP that represents the ability of the material to resist fatigue crack initiation at a given material point. Consider that both the FIP and critical FIP are random variables, where the uncertainties are expressed as probability density functions (PDF). We indicate the measure of risk as the probability of fatigue nucleation (P_{FN}). The expression of P_{FN} is given by [43]:

$$P_{\mathrm{FN}}(t) = \int_0^{\infty} \Big[\int_0^{\xi} f_R(r)dr \Big] f_S(\xi, t)d\xi = \int_0^{\infty} F_R(\xi) f_S(\xi, t)d\xi \tag{1}$$

where $F_R(\xi)$ is the cumulative distribution function (CDF) of the critical FIP, $f_R(r)$ is the PDF of the critical FIP, and $f_S(\xi)$ is the PDF of the FIP. The time dependency of the risk measure stems from the fact that increasing the number of load cycles increase the values of FIP, thereby shifting its evolving PDF as a function of time.

The overall structure of the UQ framework is schematically demonstrated in Fig. 1. The SVE concept is employed in the current study to capture the variability in the mechanical response and the FIP as a function of loading. The framework utilizes two types of experimental data: (1) microstructure morphology and material properties; and (2) fatigue nucleation life curves. The statistical microstructure morphology data are used to create a parameterized representation of the microstructural features (e.g., grain orientation and size distributions, phase volume function, etc. measured from EBSD scans and imaging of physical specimens [66]). The SVEs are generated synthetically based on parametric and probabilistic descriptions of microstructural features. The inherent variability in these features are captured by the experimental data, and the probability distributions for the parameters associated with each feature are constructed. For each feature, realizations are sampled from these distribution functions using the Monte Carlo technique. Sampled features serve as inputs to the polycrystal generation software package Neper [58], which builds the SVE geometry.

An important consideration is selecting the correlated values of SVE size (the physical

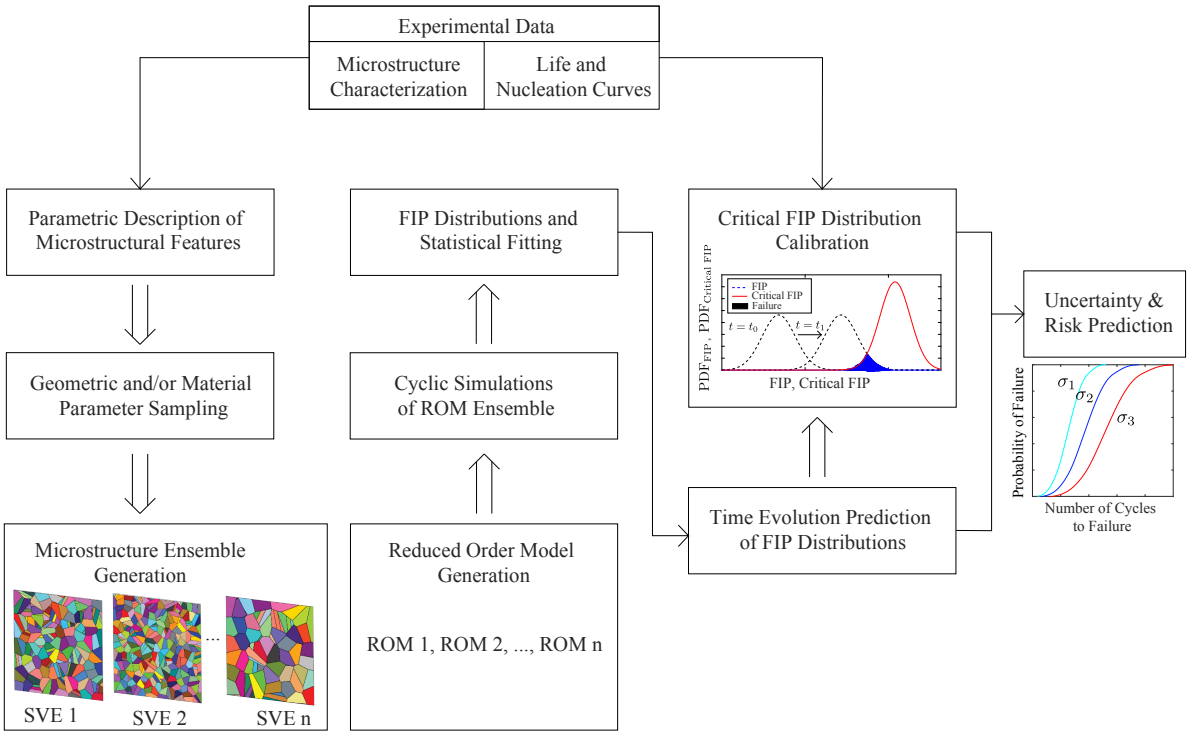

Figure 1: Overview of the proposed uncertainty quantification framework.

dimension of the SVE) and the ensemble size (the number of SVEs simulated). When the computational cost of the model that predicts the mechanical response of an SVE is high, selection of the SVE size and the ensemble size may be limited by the practical consideration of computation and time resources. In the current study, the ensemble size is determined by the convergence of the statistics of the mechanical response for a prescribed SVE size. The convergence metric we employed in this study ensures that the discrepancy between FIP distributions computed using separately sampled SVE ensembles of the same size are within a prescribed tolerance.

The numerical simulations of the mechanical behavior of SVEs serve as the bridge between microstructure morphology and fatigue nucleation prediction under cyclic loading. While direct CPFE simulations of the SVEs provide highly accurate predictions of the local fields and stress risers within microstructures, computational costs of these simulations are typically too high to directly simulate the evolution of the response as a function of loading under high cycle regime and perform sufficient number of SVEs needed for probabilistic analysis. Instead we employ a sparse implementation [79] of the eigenstrain based homogenization method (EHM) [78]. EHM is a reduced basis approximation of a CPFE simulation that allows accurate estimation of local and global response fields at a fraction of the cost of CPFE simulations [40]. In EHM, the response fields are represented as a function of a series of influence functions, obtained by

linear elastic analyses of the SVE. Coupled with a reduced basis approximation of inelastic strains and stresses, the equilibrium is approximated using a small system of nonlinear algebraic equations. This system is solved for a set of stress and inelastic strain fields averaged over SVE subdomains (or parts) in terms of coefficient tensors that retain the morphological information of the material. This approach has been shown to accurately describe small strain as well as large deformation response of polycrystals. A summary of the governing equations are provided in Section 4. For each SVE in the ensemble, the geometry is discretized, and the influence functions and coefficient tensors are computed to construct the reduced order model (ROM).

The ROMs are then exercised to simulate the spatio-temporal evolution of the response field within the SVEs. In view of the viscoplastic deformations within the microstructure, the microstructural response fields and hence FIPs continue to evolve as a function of load cycles. While the EHM approach allows for direct evaluation of several hundreds to thousands of cycles, evaluation of the high cycle fatigue response is computationally prohibitive in the context of a probabilistic framework. A time acceleration methodology [16, 17] is necessary to predict the long term evolution of the material response. In this study, the long term behavior is estimated in a statistical sense based on extrapolation of early (i.e., first few thousand cycles) evolution of the FIP probability densities. The FIP distribution computed from the SVE ensemble under the cyclic loading is fitted with an extreme value distribution (two parameter Weibull) and its evolution is extrapolated to predict the state of the distribution as a function of load cycles.

The critical FIP distribution refers to the uncertainty in the resistance of the material to fatigue nucleation. Direct experimental measurement of this critical distribution is not a trivial task. Instead, we identify this property based on experimental fatigue life measurements. The critical FIP distribution is obtained through numerical optimization, where the experimentally-observed and numerically simulated probability of fatigue nucleation is minimized for a prescribed load amplitude. The calibrated distribution along with the numerical simulation framework are exercised to predict nucleation life under different load conditions.

3 Titanium Alloy, Ti-6242

Ti-6242 is a near-α titanium alloy that has been widely used in aerospace and other engineering applications for its high specific strength, fracture toughness, high temperature capability and creep resistance. Fatigue life of near-α and $\alpha-\beta$ titanium alloys are well known to exhibit significant sensitivity to microstructural features [37]. Depending on the thermo-mechanical processing route, various types of microstructures are achieved, such as Widmanstatten, fully lamellar, bi-modal or duplex, and equiaxed α-dominated microstructures [41, 25]. Colony

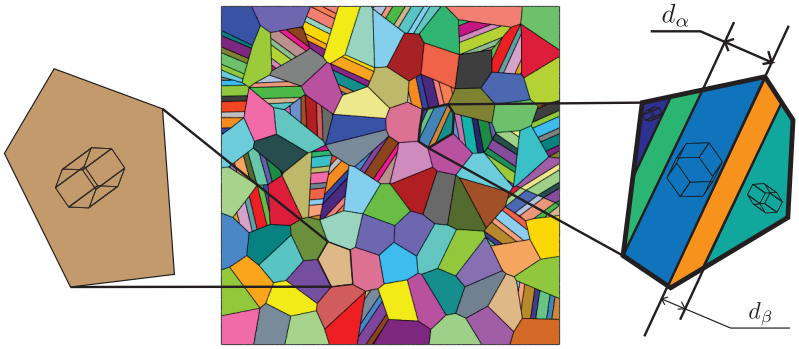

Figure 2: Schematic example of microstructure features.

grains consist of α-phase lamellae within large β-phase grains of several hundred microns in diameter. Increase in cooling rate leads to the reduction of colony grain size, α lamellae thickness, and the nucleation of new colonies, which produces the formation of "basket weave" or Widmanstatten microstructure [63]. In the current investigations, we incorporated both lamellar and pure α grains in the microstructure to model a wide range of morphology variations, and their effect on the probability of fatigue nucleation.

3.1 Microstructural features

The effects of Ti-6242 microstructure have been investigated with respect to features (pure α grain size, colony grain, lamellae structure, micro-texture etc.) through experiments (e.g., [15, 41, 60]) and numerical simulations (e.g., [4, 19, 83, 84]). A schematic illustration of bimodal Ti-6242 microstructure is shown in Fig. 2. Two types of grains are considered: pure α grain and colony grain. A colony grain is made of a collection of fine laths of alternating α phase and β phase. Each pure α grain is idealized as a single crystal, while each colony grain contains multiple α variants with prescribed thickness (d_α) and β lath with prescribed thickness (d_β). Particularly, four feature parameters of Ti-6242 are taken into account in this study: crystal orientation of prior β grain, colony grain volume fraction, α lath thickness and β lath thickness.

Orientation of α phase at room temperature depends on the metallurgical high temperature state, i.e., the parent β phase. After a heat treatment in the parent β phase, the resulting α texture does not contain variant selection, i.e., all variations have equal chances to be generated. However, with a mechanical deformation in the parent β phase, the volumes of α phases at room temperature are unbalanced. Therefore, the mechanical deformation and orientation of the prior β grain influence the crystal orientations of the α phases in the microstructure. Notwithstanding various potential mechanical deformations [41], in the current manuscript, we consider the rolling induced mechanical deformation. In this study, we consider that a SVE

domain is occupied by a single prior β grain , and the orientation of the β grain is random.

The prior β orientation is represented using three Euler angles $\{\Theta_1^\beta, \Theta_2^\beta, \Theta_3^\beta\}$. The orientation relationship between the room temperature α phase and high temperature β phase is defined by Burgers Orientation Relationships (BOR): (1) $(110)_\beta /\!/ (0001)_\alpha$ and (2) $[\bar{1}1\bar{1}]_\beta /\!/ [2\bar{1}\bar{1}0]_\alpha$ [65]. Therefore, orientation of an α grain or an α lath is selected out of 12 possible orientations relative to the orientation of the prior β grain. In fact, only a small subset of the variants are probable under different thermo-mechanical conditions. In the current study, variant selection is performed using the approach proposed by Gey et al. [23]. Denoting the orientation of i^{th} α variant as g_i^α and the orientation of the prior β grain as g^β, then

$$g_i^\alpha = \{b_i g^\beta\}_{i=1,2,...,12} \tag{2}$$

where b_i is the BOR for the i^{th} variant. The volume of the i^{th} α phase related to the volume of the prior β grain $f^\beta(g^\beta)$ by

$$f_i^\beta = v_i \cdot f^\beta(g^\beta) \tag{3}$$

and v_i is the variant selection function defined by

$$v_i = \frac{|\gamma_i|}{\sum_{\gamma_0}^{\gamma_{\max}} |\gamma|} \tag{4}$$

where γ_i is the resolved shear strain for the i^{th} variant, $\gamma_0 = X\%\gamma_{\max}$ is the minimum resolved shear strain amplitude that corresponding α variant is possible to form, and $\gamma_{\max}$ is the maximum resolved shear strain amplitude among all slip systems under given thermo-mechanical loading. The denominator sums the slip rates for which the amplitudes are larger than γ_0. This equation is based on the assumption that the orientations of α grains are distributed according to the shear strains in the corresponding slip systems, and γ_0 is the threshold shear strain. Following [23], X is selected as 50.

3.2 Uncertainty in microstructure

The sources of the uncertainties in the parameters are two fold. First is the variability observed in microstructures built using identical thermo-mechanical processing (TMP) conditions. The second is the variability in samples built by different TMP conditions. While the latter source of uncertainty is reducible, access to precise TMP conditions of the experimental samples are not often readily available and well-documented. We therefore consider the presence of both sources of uncertainties.

Table 1 shows the summary of measured values and values used in numerical studies for the microstructure geometry parameters that were used to bound the uncertainties. Deka

Table 1: Measured values of the microstructure geometry parameter for Ti-6242 available in the literature.

Reference	[19]	[30]	[57]	[60]	[31]	[4]	[83]	[84]	[68]
V_α	0.7	0.9	0.9						
d_α (μm)				0.7, 2.0, 5.9	2.0 , 3.7	1,2,5			2.5
d_β (μm)				0.2	0.5 , 0.8	0.5	0.6, 1.5, 2.5	1.6, 3.2	

Table 2: Morphology parameters.

Variable	Lower bound	Upper bound
V_α	0.65	0.95
d_α	2.0 μm	6.0 μm
d_β	0.5 μm	2.0 μm
$\theta_1^\beta, \theta_2^\beta, \theta_3^\beta$	0°	90°

et al. [19] measured the volume fraction of the transformed β phase and primary α grain in the overall Ti-6242 microstructure to be 30 percent and 70 percent, respectively. Within the colony grains, α and β lamellae were experimentally observed to have volume fractions of approximately 88% and 12%, respectively. However, measured values for the volume fraction of α and β phases of Ti-6242 are 90 percent and 10 percent in the experiments by Jun et al. [30] using secondary electron micrographs. Similarly, the volume fraction of α grains in the Ti-6242 specimens is approximately 90 percent in the experiments conducted by Qiu et al. [57]. The grain size of α grains is approximately 13.6μm. Sansoz and Ghonem [60] performed scanning electron microscope examinations on the fracture surface of three microstructures in order to identify the relevant crack growth mechanisms with respect to the microstructure details. In these three microstructures, the average thicknesses of α laths are quite different (0.7, 2.0 and 5.9 mm), while the average thickness of the β lath is found to be similar in all produced microstructures (0.2 mm). Jun et al. [31] studied local deformation mechanisms in Ti-6242 by performing in-situ micropillar compression tests on nine different pillars, and they concluded that, for the colony structures, the presence and morphology of the β phase can significantly alter the apparent yielding point and work hardening response. The widths of α and β lath in their specimens were approximately 2 mm and 0.5 mm, while the averaged thicknesses in the nine processed specimens were around 3.7 mm and 0.8 mm for α and β lath, respectively.

The range of values observed in the aforementioned experimental observations are used herein to bound the ranges of microstructure geometry model parameters. Table 2 summarizes the bounds used for all parameters. Since no distributional information is available, the parameters are considered to be uniformly distributed within these bounds.

Table 3: Parameters of the FCG model.

Parameter	x_0	x_1	x_2	x_3	α_1
Value	$\ln 3.5$	$\ln 5.0$	$\ln 25$	$\ln 47.1(1-R)$	-0.0808
Parameter	β_1	C	m	α_3	β_3
Value	0.0023	7×10^{-9}	3.3	1.8938	3.3

3.3 Uncertainty in fatigue life

To estimate the fatigue nucleation life based on total fatigue lives reported in experimental samples, the fatigue crack growth (FCG) model developed by Shen et al. [62] is used. Three stages of fatigue failure (crack initiation, crack propagation and final rupture) are all taken into account in the employed FCG equations. The fundamental idea is to solve for the cycle number of fatigue nucleation given the experimentally observed fatigue failure life, i.e., the inverse of problem of FCG. The initial crack length at fatigue nucleation is taken to be 0.1 mm following [45]. In the current manuscript, Paris' parameters (C and m) and fracture toughness are the taken to be same as in Ref. [62], while the other model parameters are re-computed based on the values and continuity conditions provided in the reference. The model parameters used in this study are summarized in Table. 3. x_0, x_1, x_2 and x_3 are the transition points between fatigue regimes. x_3 is computed from to the fracture toughness (47.1 MPa$\sqrt{\text{m}}$) and R ratio, where x_0, x_1 and x_2 are estimated from experiments. α_1 and β_1 are material constants and obtained through the continuity conditions of crack growth rate and its first order derivative at x_1. α_3 and β_3 describe material behavior at high ΔK regime, and are calculated from the continuity conditions at x_2.

Several studies report experimentally measured number of cycles to failure N_f for Ti-6242 at various stress levels. Fujishiro and Eylon [21] investigated the effect of Pt ion plating on the high cycle axial fatigue life of Ti-6242 specimens at room temperature and 455°C. Measured number of cycles to failure at room temperature without Pt coat are employed in this study. Yuan et al. [76] studied the effects of surface roughness and residual stress induced by the mechanical polishing treatments (cold rolling polishing (CRP), sandpaper polishing (SP) andnylon cloth polishing (NCP)) on fatigue life. Sinha et al. [64] presented the results of a study of the response of an β-forged Ti-6242 during static, normal-fatigue, and dwell-fatigue loading. Results under pure fatigue loading is employed in the current study. Ghosh et al. [24] conducted pure fatigue and dwell fatigue tests with different test conditions (load ratio, dwell time and peak stress to yield strength ratio) for the three α/β-forged and one β-forged Ti-6242. Ref. [49] provided the fatigue properties of duplex annealed sheet at room temperature and smooth rotating beam made of Ti-6242. However, available data points are limited to relative low stress level ($< 90\%$ yield stress). Pilchak et al. [54] performed fatigue test on both

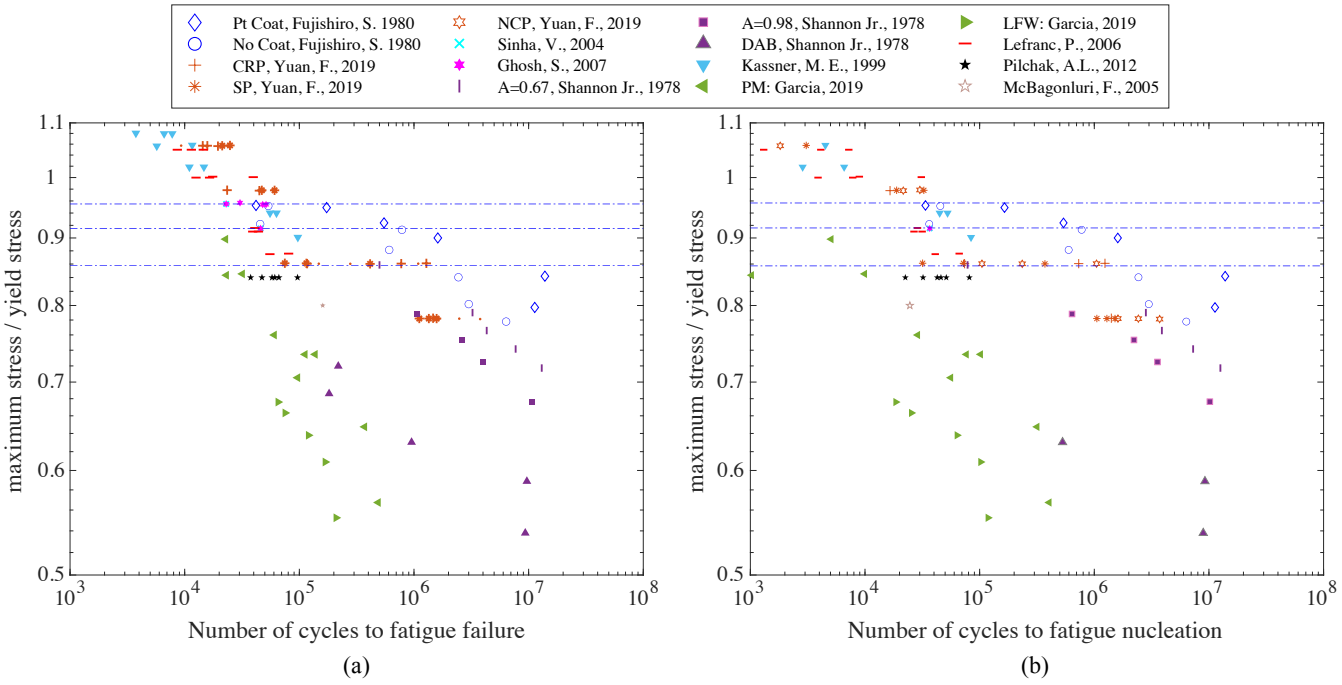

Figure 3: (a) Experimental fatigue failure data available in the open literature; and (b) nucleation life estimated based on the experimental life data and the FCG model. The dashed lines represent three stress levels investigated in the numerical analysis.

as-received samples and exposed samples at 80% yield strength. Kassner et al. [32] determined the low cycle fatigue properties and dwell low cycle fatigue properties for Ti-6242. Garcia and Morgeneyer [22] measured the fatigue life for the parent material (PM) and linear friction welds (LFW) of Ti-6242, and number of cycle to failure is observed mainly with stress less than 800 MPa. Lefranc et al. [36] focused the dwell effect on β-forged Ti-6242, but they also measured fatigue life for comparison. The experimental data collected in the aforementioned studies have been compiled and plotted in Fig. 3a. We note that the experimental conditions in these studies (e.g., stress ratio, air/vacuum exposure, testing equipment) are not necessarily identical. The fatigue nucleation data that is generated by subtracting the long crack growth and rupture lives by using the FCG model from the experimental data are shown in Fig. 3b.

4 Methodology

4.1 DD-EHM formulation

The domain of an SVE is denoted as Θ. This polycrystalline microstructure is decomposed into non-overlapping n sub-domains (or reduced order "parts"), where $\Theta^{(\mathbb{A})}$ denotes the domain of part $\mathbb{A}$. In the current study, the domain of each pure α grain as well as each lath within

the colony grains constitute a part. We denote $\dot{\sigma}^{(\mathbb{A})}$ and $\dot{\mu}^{(\mathbb{A})}$ the part average (i.e., over $\Theta^{(\mathbb{A})}$) stress rate and plastic deformation rate, respectively. The EHM formulation expresses equilibrium using the following relationship:

$$M^{\mathbb{B}}_{ijkl}\dot{\sigma}^{(\mathbb{B})}_{kl}(\boldsymbol{x},t) - \sum_{\alpha=1}^{n}\left[P^{(\mathbb{B}\mathbb{A})}_{ijkl} - \delta^{(\mathbb{A}\mathbb{B})}I_{ijkl}\right]\dot{\mu}^{(\mathbb{A})}_{kl}(\boldsymbol{x},t) = A^{(\mathbb{B})}_{ijkl}\dot{\bar{\epsilon}}_{kl}(\boldsymbol{x},t) \tag{5}$$

in which, $\dot{\bar{\boldsymbol{\epsilon}}}$ is the SVE-averaged strain rate, $\boldsymbol{M}^{(\mathbb{B})}$ is the elastic compliance tensor of the constitutive occupying $\Theta^{(\mathbb{B})}$, $\boldsymbol{P}^{(\mathbb{B}\mathbb{A})}$ and $\boldsymbol{A}^{(\mathbb{B})}$ are interaction and concentration tensors, respectively. $\boldsymbol{P}^{(\mathbb{B}\mathbb{A})}$ and $\boldsymbol{A}^{(\mathbb{B})}$, collectively named coefficient tensors, are computed from elastic influence functions associated with the SVE. $\dot{\bar{\boldsymbol{\epsilon}}}$ constitute the forcing function and prescribed to apply the cyclic loading.

Equation 5 is evaluated alongside crystal plasticity models (detailed below) that describe the evolution of part-averaged plastic deformations. The constitutive laws are therefore expressed in terms of part-averaged quantities. Since the constitutive equations are nonlinear, the EHM formulation results in a nonlinear algebraic system of $6n$ equations to describe the SVE response. Since all $P^{(\mathbb{B}\mathbb{A})}$ are non-zero, the resulting system is dense and scale badly for large n. In order to reduce cost for problems with large n, we employ a sparse formulation where long range grain interactions are ignored [79].

In simulations below, fatigue loading is defined in terms of stress rather than strain. In order to ensure that proper load amplitude is applied at each cycle, a stress-controlled incrementation scheme is implemented, where the strain rate is kept until a peak SVE-average stress is reached and then reversed to begin unloading. The SVE-averaged stress is computed as

$$\overline{\sigma}_{ij} = \sum_{\mathbb{B}=1}^{n} v^{(\mathbb{B})}\sigma^{(\mathbb{B})}_{ij} \tag{6}$$

where $v^{(\mathbb{B})}$ is the volume fraction of part $\mathbb{B}$.

4.2 Constitutive model

A dislocation-mediated crystal plasticity model [39] has been adopted to describe the evolution of viscoplastic deformation within each subdomain, $\Theta^{(\beta)}$. To simplify notation, we do not use part designation in the geometry equations below. The slip rate at the s^{th} system is derived from the Orowan's equation:

$$\dot{\gamma}^s = \frac{\rho^s_{\text{m}} v^s_{\text{id}} (b^s)^2}{2}\text{sign}(\tau^s)\exp\left\{\left(\frac{-\Delta F^s}{k\theta}\right)\right\}\exp\left\{\left(\frac{(\tau^s - s^s)\Delta V^s}{k\theta}\right)\right\} \tag{7}$$

where ρ^s_{m} is the average mobile dislocation density, v^s_{id} the vibration frequency of the dislocation segment, b^s the magnitude of the Burgers vector, k the Boltzmann constant and θ the temperature in Kelvin, ΔV^s the thermal activation volume, and ΔF the activation energy. s^s is the critical resolved shear strength, and the strength hardening is expressed as

$$s^s(\dot{\gamma}^s) = s^s_0 + s^s_{\mathrm{for}}(\dot{\gamma}^s) + s^s_{\mathrm{deb}}(\dot{\gamma}^s) \tag{8}$$

where s^s_0 is the initial slip resistance, $\dot{\gamma}^s$ is the slip rate at s^{th} slip system, s^s_{deb} and s^s_{for} denote the contributions to strength evolution by dislocation debris and forest dislocations, respectively. In the current manuscript, the evolution of the debris dislocation is related to the recovery process induced by dislocation climb or cross-slip, and the hardening is affected by debris dislocation on all slip systems. The evolution of the forest dislocation is controlled by the competing mechanisms of generation and annihilation associated with recovery.

The contributions by dislocation debris and forest dislocations to strength evolution are denoted as s^s_{deb} and s^s_{for} respectively.

$$s^s_{\mathrm{for}}(\dot{\gamma}^s) = \mu\chi b^s\sqrt{\rho^s_{\mathrm{for}}} \tag{9}$$

$$s^s_{\mathrm{deb}}(\dot{\gamma}^s) = \mu b^s k_{\mathrm{deb}}\sqrt{\rho_{\mathrm{for}}}\ln\left(\frac{1}{b^s\sqrt{\rho_{\mathrm{deb}}}}\right) \tag{10}$$

where μ is the shear modulus, χ is the dislocation interaction parameter, b^s is the Burgers vector. ρ^s_{for} and ρ^s_{deb} represent the forest and debris dislocation density, respectively. k_{deb} is the material independent factor associated with low substructure dislocation density.

The total forest dislocation density is expressed as:

$$\rho^s_{\mathrm{for}} = \rho^s_{\mathrm{fwd}} + \rho^{s+}_{\mathrm{rev}} + \rho^{s-}_{\mathrm{rev}} \tag{11}$$

where ρ^s_{fwd} is the forward dislocation density and $\rho^{s\pm}_{\mathrm{rev}}$ denote the reversible terms corresponding to loading and unloading paths along the s_{th} slip system. Back stress was previously introduced to describe dislocation interactions [61], which is inversely proportional to the dislocation density. The incorporation of back-stress component can capture Bauschinger effect. In this study, the dislocation-dislocation interaction, specifically dislocation annihilation, was directly incorporated through dislocation evolution, i.e. reversible dislocation. The reversible dislocation density decreased during reversal of resolved shear stress and this has been demonstrated to capture Bauschinger effect in Refs. [33, 40]. The evolution of the forward dislocation density includes both athermal storage and temperature dependent recovery of classical Kock-Mecking law, as given below:

$$\frac{\partial\rho^s_{\mathrm{fwd}}}{\partial\gamma^s} = (1-p)k^s_1\sqrt{\rho^s_{\mathrm{for}}} - k^s_2(\dot{\gamma},\theta)\rho^s_{\mathrm{for}} \tag{12}$$

where p is a reversibility parameter. k_1^s controls the generation of forest dislocations, and the recovery coefficient k_2^s is taken to be:

$$k_2^s(\dot{\gamma}, \theta) = k_1^s \frac{b^s \chi}{g^s}(1 - \frac{k\theta}{\hat{D}^s b^{s^3}} \ln \frac{\dot{\gamma}^s}{\dot{\gamma}_0}) \tag{13}$$

where $\dot{\gamma}_0$, g^s and $\hat{D}^s$ are the reference shearing rate, effective activation enthalpy and drag stress, respectively. The evolution of the remaining two components, ρ_{rev}^{s+} and ρ_{rev}^{s-} are expressed as functions of loading direction in the slip system:

$$\frac{\partial \rho_{\text{rev}}^{s+}}{\partial \gamma^s} = \mathbb{H}\big(\text{sign}(\tau^s)\big)\Big(pk_1^s\sqrt{\rho_{\text{for}}^s} - k_2^s(\dot{\gamma}^s, \theta)\rho_{\text{rev}}^{s+}\Big) + \mathbb{H}\big(\text{sign}(-\tau^s)\big)\Big[-k_1^s\sqrt{\rho_{\text{for}}^s}(\frac{\rho_{\text{rev}}^{s+}}{\rho_0^s})^{\hat{m}}\Big] \tag{14}$$

$$\frac{\partial \rho_{\text{rev}}^{s-}}{\partial \gamma^s} = \mathbb{H}\big(\text{sign}(\tau^s)\big)\Big(-k_1^s\sqrt{\rho_{\text{for}}^s}(\frac{\rho_{\text{rev}}^{s-}}{\rho_0^s})^{\hat{m}}\Big) + \mathbb{H}\big(\text{sign}(-\tau^s)\big)\Big[pk_1^s\sqrt{\rho_{\text{for}}^s} - k_2^s(\dot{\gamma}^s, \theta)\rho_{\text{rev}}^{s-}\Big] \tag{15}$$

where $\mathbb{H}$ is the heaviside function, ρ_0^s the total dislocation density at the point of load reversal, $\hat{m}$ the dislocation density recombination coefficient.

The evolution of the debris dislocation density is expressed as:

$$d\rho_{\text{deb}} = \sum_s \frac{\partial \rho_{\text{deb}}^s}{\partial \gamma^s} d\gamma^s, \quad \text{and} \quad \frac{\partial \rho_{\text{deb}}^s}{\partial \gamma^s} = qb^s\sqrt{\rho_{\text{deb}}}k_2^s(\dot{\gamma}^s, \theta)\rho_{\text{for}}^s \tag{16}$$

where q is the recovery rate coefficient.

4.3 Fatigue indicator parameter

The mechanical behavior of the Ti-6242 microstructure under repeated cyclic loading is predicted by the Sparse DD-EHM, while the onset of fatigue is indicated by the FIP which is a function of microscale information (plastic strain, energy etc). A number of FIPs have been previously proposed to predict fatigue initiation life of polycrystalline materials. Przybyla and McDowell [56] employed the maximum plastic shear strain range (MPSS) and Fatemi-Socie (FS) damage parameter to investigate driving forces for fatigue crack formation at the scale of microstructure. Li et al. [38] developed a fatigue parameter based on accumulated plastic strain accounting for triaxiality and temperature effects to predict thermo-mechanical fatigue. Sangid et al. [59] proposed an energy-based failure criterion to link the variability in the microstructure to fatigue response.

In the context of titanium alloys, the nucleation process results in facet formation in a hard grain generally oriented along a direction near the basal plane. Liu et al. [40] proposed maximum relative dislocation density discrepancy (MD^3) as a FIP for titanium alloys, considering that dislocation pile-ups at grain boundaries induce crack nucleation. The amount of pile-ups and the inability of the dislocations cross the grain boundary are collectively quantified by

Table 4: Elastic constants for HCP and BCC crystals.

Parameter	C_{11}	C_{12}	C_{13}	C_{33}	C_{44}
BCC (GPa)	108.2	61.3	61.3	108.2	28.5
HCP (GPa)	164.66	82.5	61.7	175.1	48.5

the relative dislocation density discrepancy (D^3) across a grain boundary. MD^3 indicates the maximum value of D^3 across all grain boundaries within the SVE. Instead of focusing on a single extreme value (i.e., MD^3) over entire microstructure and history, we aggregate the spatial distribution of D^3 within each SVE of an SVE ensemble. The D^3 distribution at peak load amplitude is tracked.

The D^3 for grain i, $(\Delta\rho_{\text{tot}})^i$, is defined as the relative dislocation density discrepancy between grain i and all its neighbors.

$$(\Delta\rho_{\text{tot}})^i = \max_{j\in\{1,\dots,m_i\}} \left\{ \left| (\rho_{\text{tot}})^i - (\rho_{\text{tot}})^{k(j)} \right| \right\} \tag{17}$$

where $(\rho_{\text{tot}})^i$ is the maximum dislocation density for grain i over all slip systems, $k(j)$ is the grain ID for the j^{th} neighbor of grain i, ρ_{tot} is the total dislocation density defined as $\rho_{\text{tot}} = \rho_{\text{for}} + \rho_{\text{deb}}$.

5 Fatigue Nucleation Prediction

5.1 Constitutive model parameters

The microstructure of Ti-6242 is modeled using two types of crystals: BCC β phase and HCP α phase. To ensure that the constitutive formulation captures the response of the alloy accurately, the constitutive parameters calibrated by Liu et al. [40] are employed. The constitutive model parameters are considered to be deterministic that are calibrated using a representative volume (i.e., representative for the purposes of viscoplastic response). Specimen to specimen variability in the static stress-strain response, which influences fatigue nucleation uncertainty (especially in low cycle fatigue), has been partially explained by the uncertainty in the model parameters [59, 80, 81, 82]. Under high cycle fatigue conditions considered in this study, the effect of parameter uncertainty for elastic and viscoplastic properties is not explicitly incorporated.

The HCP model includes 30 slip systems including the basal, pyramidal and prismatic systems, and the BCC model includes 48 slip systems. All slips systems used in the model are summarized in Table. 5. The elastic parameters are listed in Table 4, and the flow and hardening parameters for both the HCP and BCC lattices are summarized in Table 6.

Table 5: Slip system of HCP and BCC.

Lattice	Type	Slip system	Number
HCP	Basal $\langle$a$\rangle$	$\{0001\}\langle 11\bar{2}0\rangle$	3
	Prismatic $\langle$a$\rangle$	$\{10\bar{1}0\}\langle 11\bar{2}0\rangle$	3
	Pyramidal $\langle$a$\rangle$	$\{10\bar{1}1\}\langle 11\bar{2}0\rangle$	6
	1$^{\text{st}}$ Order Pyramidal $\langle$c+a$\rangle$	$\{10\bar{1}1\}\langle 11\bar{2}3\rangle$	12
	2$^{\text{nd}}$ Order Pyramidal $\langle$c+a$\rangle$	$\{11\bar{2}2\}\langle 11\bar{2}3\rangle$	6
BCC		$\{110\}\langle 1\bar{1}1\rangle$	12
		$\{112\}\langle 12\bar{1}\rangle$	12
		$\{123\}\langle 11\bar{1}\rangle$	24

Table 6: Flow rule parameters for HCP and BCC crystals.

Parameter	Unit	Basal $\langle$a$\rangle$	Prismatic $\langle$a$\rangle$	Pyramidal $\langle$a$\rangle$	Pyramidal $\langle$c+a$\rangle$	$\{110\}(\bar{1}11)$
ΔF^s	$\times 10^{-19}$J	2.58	2.93	3.21	3.44	2.27
ΔV^s	$\times 10^{-29} m^3$	1.94	2.84	2.96	3.17	479
ρ^s_m	$\times 10^{12} m^{-2}$	5	5	5	5	5
v^s_{id}	$\times 10^{12} Hz$	1	1	1	1	1
b^s	$\times 10^{-4} \mu m$	3.54	3.58	3.59	6.83	2.86
s^s_0	MPa	11.6	47.2	143.69	158.87	94
k^s_1	$\times 10^{6} m^{-1}$	6.32	107	103	174	52
D^s	MPa	100	150	185	225	230

The strength hardening evolution in HCP dominated crystals is controlled by initial slip resistance, forest dislocation and debris dislocation, and corresponding parameters are summarized in Table 7. The dislocation interaction parameter χ is set as 0.9 to satisfy the Taylor relationship [8]. The material independent factor k_{deb} is set as 0.086 [42]. A small value of initial forest dislocation density is adopted, $\rho_{\text{for},0} = 1 \times 10^{12}$ m^{-2}, according to experimental observations [67, 50, 47]. The reversibility parameter p is chosen as 0.8 [33]. The reference shear strain rate $\dot{\gamma}_0$ is defined as 10^7 s^{-1}. The dislocation density recombination coefficient $\hat{m}$ is taken to be 0.4 for HCP and BCC [77]. The initial debris dislocation density in all slip systems are defined as 1×10^{10} m^{-2} [3]. With these constitutive parameters, the tensile yield stress (σ_y) of the material is computed as 875 MPa at a strain rate of 0.1/s.

5.2 SVE ensemble

The mechanical response of Ti-6242 SVEs under cyclic loading is obtained using the EHM approach. In order to facilitate uncertainty computations (i.e., reduce computational cost), SVEs are modeled as quasi 2D. The edge length of an SVE is set to 39 μm. Grain sizes are sampled from a bi-modal distribution function (lognormal distribution (sigma, mu) =

Table 7: Hardening parameters.

Parameter	χ	k_{deb}	$\rho_{\text{for},0}$	p	$\dot{\gamma}_0$	$\hat{m}$	$\rho^s_{\text{deb},0}$
Unit			m^{-2}		s^{-1}		m^{-2}
Value	0.9	0.086	1×10^{12}	0.8	10^7	0.4	1×10^{10}

(10.21, 0.16) and normal distribution with cutoff (sigma, mu) = (0.43, 1.74)) [40]. Morphology parameters shown in Table 2 are randomly sampled, SVEs generated and discretized, and coefficient tensors are computed to build a ROM for each SVE.

The SVEs were subjected to stress controlled tensile loads with an R-ratio of 0.1 and load frequency of 1 Hz Viguier et al. [67]. For each SVE within the ensemble, the fatigue indicator parameter (i.e., D^3) at every grain interface was computed as a function of load cycles. The D^3 values were then aggregated across the ensemble to obtain the D^3 distribution and its time evolution.

The effect of SVE ensemble size and the SVE size on predicted D^3 distribution are determined through a numerical convergence study. In order to quantify the effect of ensemble size, we performed a pool of 10,258 SVE simulations. The size of the pool is selected large enough so that the D^3 distribution for the entire pool could be considered representative and converged. All ensembles were then generated by random sampling from the SVE pool. All simulations were performed using NASA's Pleiades supercomputer. Each SVE simulation in the pool was subjected to 10 cycles of loading with load amplitude of $\text{X}\%\sigma_y$. D^3 values were extracted from the end of the load cycle. The PDFs and CDFs of D^3 distributions for ensemble sizes of 100, 250, 500, 750, 1,000 and 2,000 are shown in Fig. 4. For each ensemble size s, s SVEs are randomly selected out of the simulation pool, and this process was repeated for 50 times. These 50 separate ensembles (referred to as ensemble samples) were used to quantify the variation in D^3 distributions. The results demonstrate a clear narrowing trend in the variations with increasing ensemble size, which confirms the expectation that increased ensemble size allows a more thorough sampling leading to less ensemble-to-ensemble variation. We further contend that large ensemble sizes are necessary to achieve sufficient sampling of the extreme value statistics. It is possible to reduce the demand on the ensemble size by increasing the size of the SVE instead. However, larger ensembles of smaller SVEs are computationally less costly as SVE simulations in the ensemble can be performed in parallel with linear scalability, whereas evaluation of a single SVE simulation in parallel typically scales sublinearly with size. In the current manuscript, the SVE size with 150 grains is applied for each microstructure, and we aggregate the responses in the analyses.

The ensemble-to-ensemble variability as a function of ensemble size is quantified using the Kolmogorov–Smirnov (KS) test. The Kolmogorov–Smirnov measure $D^\star$ for two arbitrary

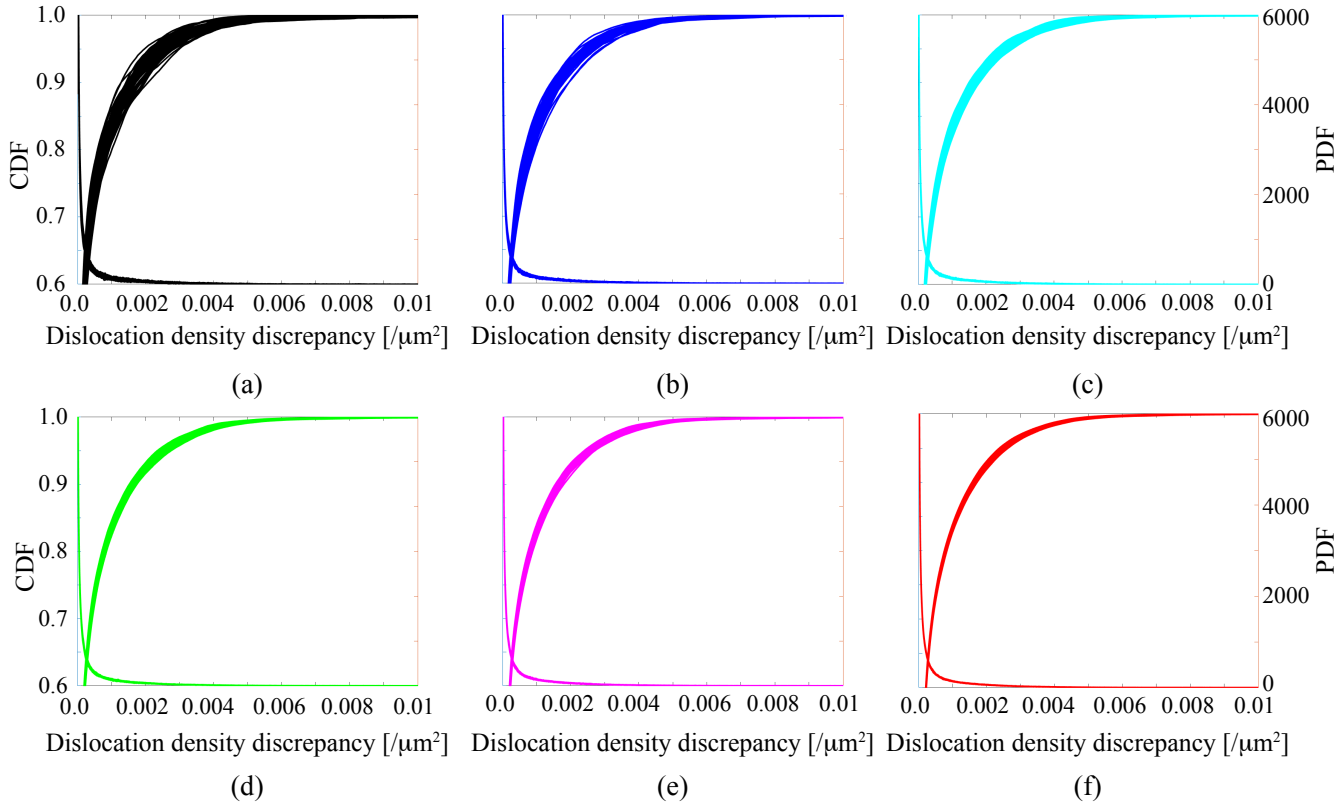

Figure 4: Variability in the cumulative and probability distributions of D^3 as a function of ensemble size (a) 100 SVEs, (b) 250 SVEs, (c) 500 SVEs, (d) 750 SVEs, (e) 1,000 SVEs and (f) 2,000 SVEs.

sample cumulative distribution functions, $F_1(x)$ and $F_2(x)$, is defined as

$$D^\star = \max_x |F_1(x) - F_2(x)| \tag{18}$$

$D^\star$ is the largest absolute difference between two CDFs. For a given ensemble size, we computed the KS measure of every pair of CDF ensemble samples, resulting in 1,225 $D^\star$ values. Figure 5a shows the PDFs of the KS statistics at different ensemble sizes and Figure 5b shows the histograms of maximum KS statistics as a function of ensemble size.

It is clear that increasing ensemble size monotonically reduces both the variance of $D^\star$ and mean of $D^\star$ distribution, confirming the converging trend of D^3 distribution with ensemble size. The maximum values of $D^\star$, which correspond to the largest difference among all 50 ensemble samples for a given size, are extracted and plotted as a function of ensemble size in Fig. 5b. Increasing the ensemble size from 100 to 2,000 significantly reduces the discrepancy between the aggregated D^3 distribution ($\sim 2\%$ for 2,000 SVEs). For an ensemble size of 500, the maximum $D^\star$ is less than 5%.

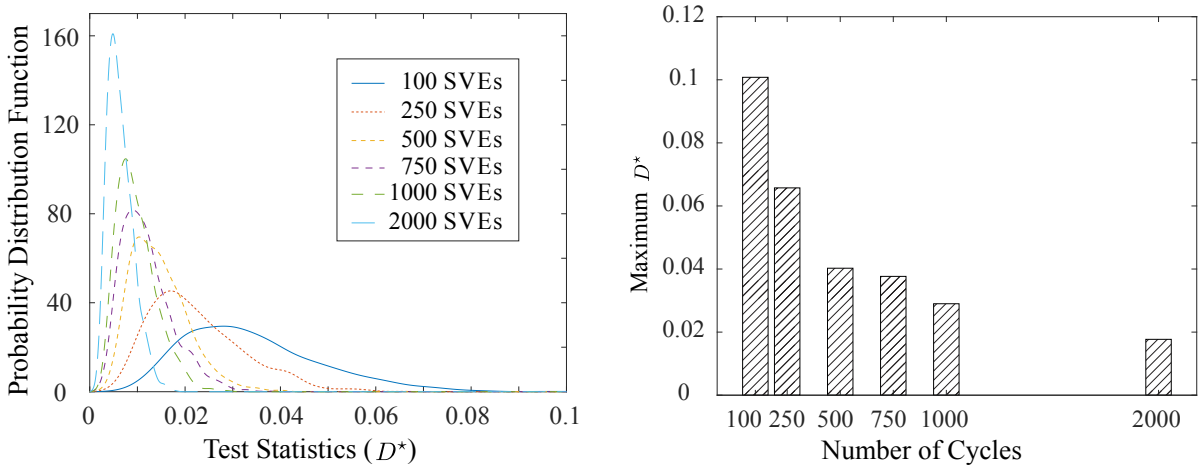

Figure 5: Distributions of D* with increasing number of SVEs, and convergence of max D* with increasing number of SVEs.

5.3 Long term evolution of FIP distributions

Tracking the evolution of the FIP distribution as a function of load cycles based on cycle-by-cycle simulation of an ensemble of SVEs is computationally prohibitive for high cycle fatigue. For instance, evaluation of a single SVE response over 1,000 load cycles using the sparse DD-EHM approach require approximately 1 CPU-day. Therefore, an extrapolation technique is employed to predict the long term evolution of FIP distribution. For the first 1,000-2,000 cycles, the distribution of FIP is predicted by the sparse DD-EHM approach for SVE ensembles. The particular number of cycles to simulate at a given load amplitude is chosen such that the rate of change of the FIP distribution is at a steady state. For response at larger cycle numbers, the FIP distributions are fitted to parameterized extreme value distributions with parameters extrapolated from the sparse DD-EHM predictions.

In the current study, five hundred SVEs are selected to represent the 10,258 SVE pool based on the selection criterion that the difference between maximum $D^\star$ of the 500 SVE ensemble and maximum $D^\star$ of the 10,258 SVE pool is smaller than the critical value ($1.36/\sqrt{n}$ for $n > 40$) in the KS test table at significance level of 0.05. Cyclic loading is applied to these 500 SVEs up to 2,000 cycles. The FIP (D^3) is represented using a Weibull distribution at any given time instance, and its evolution is tracked by the evolution of the Weibull parameters (shape parameter and scale parameter). The Weibull distribution was selected due to the better capture of tail of probability plot, as shown in Fig. 6.

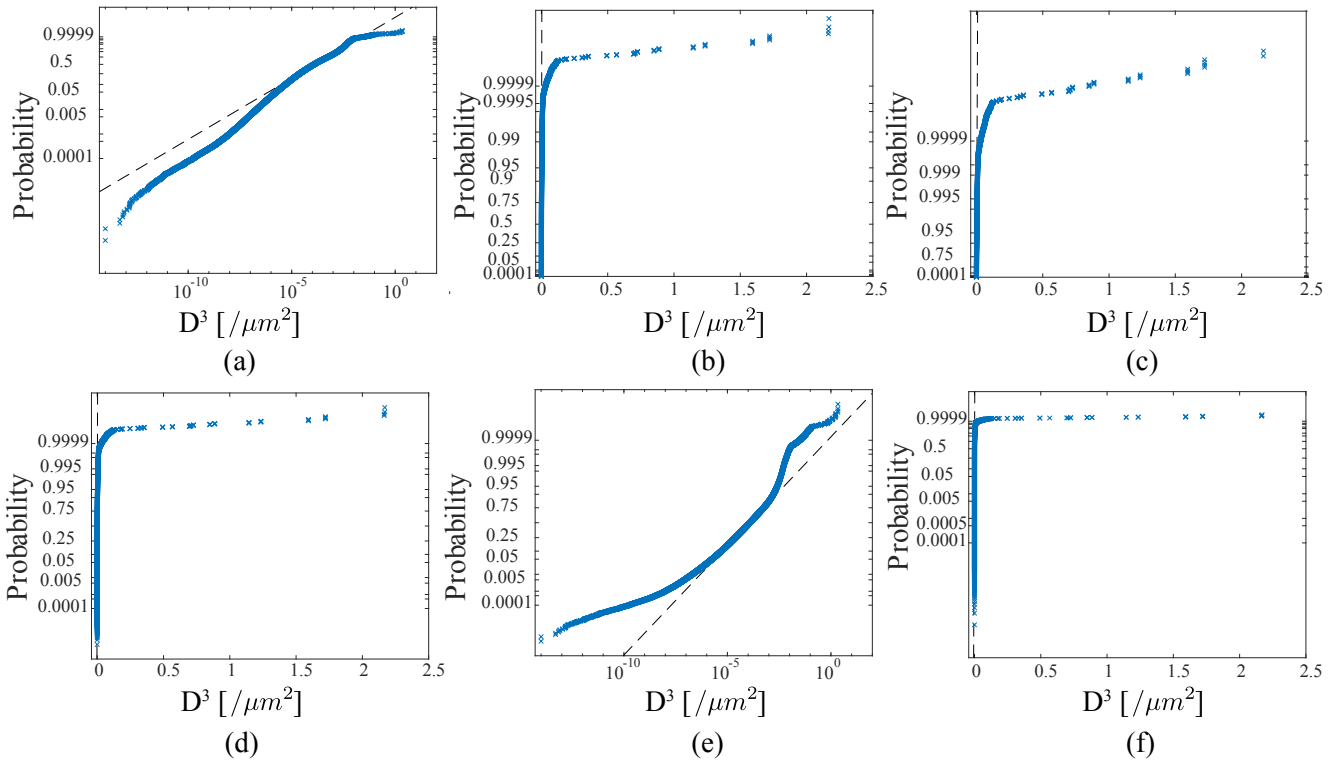

Figure 6: Distribution fits for (a) Weibull, (b) Rayleigh, (c) exponential, (d) normal, (d) lognormal and (f) extreme value models.

The probability distribution for a Weibull random variable is expressed as:

$$f(x;\lambda,k) = \begin{cases} \frac{k}{\lambda}(\frac{x}{\lambda})^{k-1}\exp\{[-(\frac{x}{\lambda})^k]\} & x \geq 0 \\ 0 & x < 0 \end{cases} \tag{19}$$

where $k > 0$ is the shape parameter, and $\lambda > 0$ is the scale parameter.

At 91.5% yield stress, the distributions at 100 cycles, 200 cycles, 500 cycles and 1000 cycles are shown in Figure 7. The Weibull distribution captures the tail of D^3 distribution for $D^3 > 10^{-5}$ reasonably well for all time instances. The D^3 distributions shift towards higher D^3 with increasing number of load cycles. It may also be possible to obtain reasonable fits with other distributions such as Gumbel or Frechet distributions, which were suggested in some previous studies [55].

To estimate the evolution of D^3 distribution between 1,000 cycles to 100,000 cycles or higher, the parameters of Weibull distribution are expressed in a function form that varies with the number of load cycles. The temporal evolution of the shape and scale parameters within the first 1,000 or 2,000 cycles as computed directly by the SVE simulations, and as fitted to a bilinear curve are shown in Fig. 8. Figure 8a and b respectively shows the evolution of scale

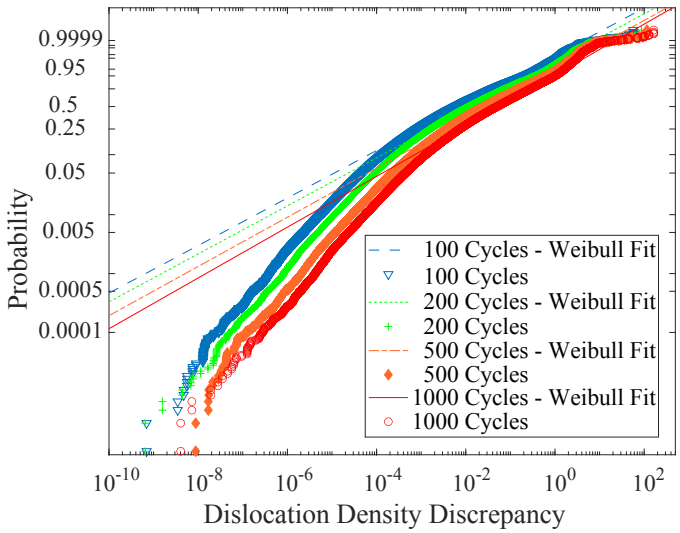

Figure 7: Motion of D^3 distribution.

and shape parameters at three stress levels (85.8%, 91.5% and 95.5% yield stress) as a function of cycle number. The time evolution of the scale and shape parameters obtained from SVE simulations are indicated by circle, triangle and diamond symbols. In these plots we observe, (i) the initial quick increase of local dislocation density mismatch, due to rapid dislocation density accumulation at the onset of plastic deformation followed by (ii) stable dislocation accumulation due to strain hardening in CRSS, leading to a stable slip accumulation and dislocation density accumulation. Capturing the second stage (i.e., the slope of the curves in the second stage) is particularly important as it is projected to continue for a large number of cycles. A bilinear curve is the simplest curve that is able to fit the observed behavior. The bilinear fits capture the SVE data well particularly at large number of cycles, where the evolutions of the parameters stabilize. A change in the scale parameter affects on the distribution as a change of the abscissa scale. The reduction in the value of the scale parameter while keeping the shape parameter constant results in the narrowing of the distribution. As indicated in Fig. 8a, higher stress level has larger scale parameter therefore larger variation in D^3 distribution.

5.4 Critical FIP calibration and model validation

Direct experimental observations of the fatigue indicator parameter at fatigue nucleation are not available at the material microstructure scale. The calibration of the critical D^3 distribution is performed by minimizing the discrepancy between the measurements of fatigue life and model predictions at a prescribed load amplitude (i.e., 91.5% of yield stress). The calibrated critical FIP distribution is then validated by comparing the model predictions and experimen-

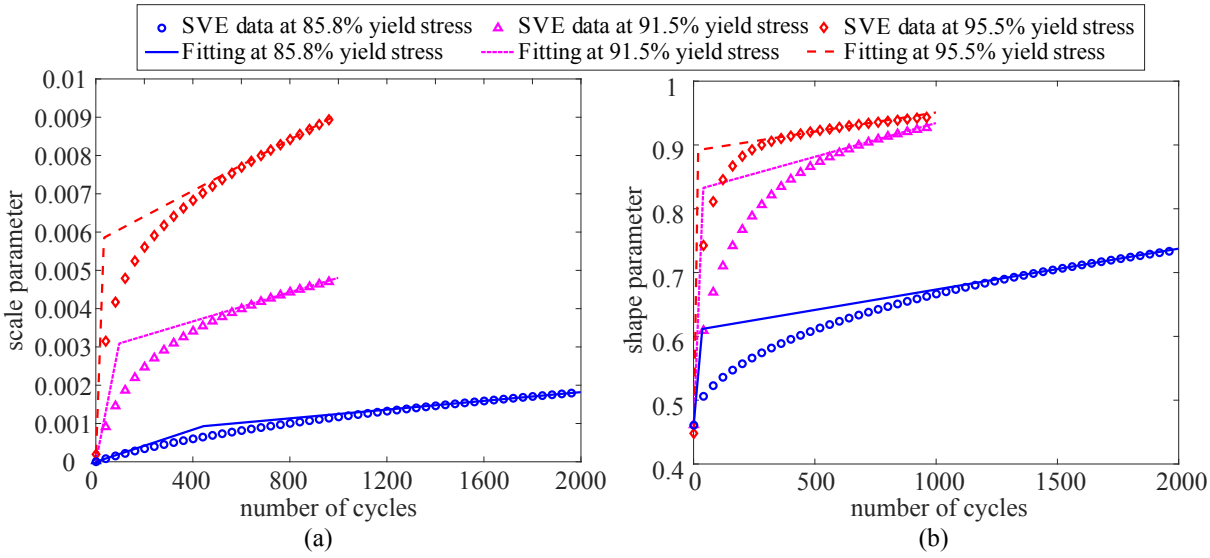

Figure 8: Temporal evolution of (a) the scale parameter and (b) the shape parameter.

tal life curves at other load amplitudes (i.e., 95.5% and 85.8% of yield stress). 91.5% of yield stress load amplitude was used in the calibration because larger number of experimental data points are available for this load level compared with the other load levels. The calibration was performed using numerical optimization by minimizing the discrepancy in the probability of fatigue nucleation expressed as:

$$R_{P_{\mathrm{FN}}} = \sqrt{R_1^2 + R_2^2 + ... + R_{n_{cp}}^2} \tag{20}$$

where R_i is the difference between the predicted P_{FN} and experimental P_{FN} at the i^{th} data point, and n_{cp} is the number of calibration points. We note that since the number of experimental data points is relatively low, data were first fitted to a smooth distribution and the calibration was performed by minimizing the discrepancy between data points from the fitted distribution and the simulation results. The outcome of the calibration process is shown in Fig. 9b. The calibrated strength distribution and predicted evolution of D^3 distributions at 91.5% yield stress are plotted in Fig. 10. The motion of D^3 is represented every 5,000 cycles and up to 50,000 cycles.

Figure 9 illustrates the predicted probability of the fatigue nucleation curves are compared with those from experimental observations for load amplitudes of 85.8%, 91.5% and 95.5% of yield stress, respectively. The simulated probability of fatigue nucleation at 91.5% yield stress is from calibration and therefore exhibits high accuracy. The fatigue nucleation probabilities are slightly underpredicted for the low amplitude loading, whereas they are slightly overpredicted for the high amplitude loading. It is important to note that the total number of cycles to failure varies significantly (e.g., more than an order of magnitude between 85.8% and 91.5%

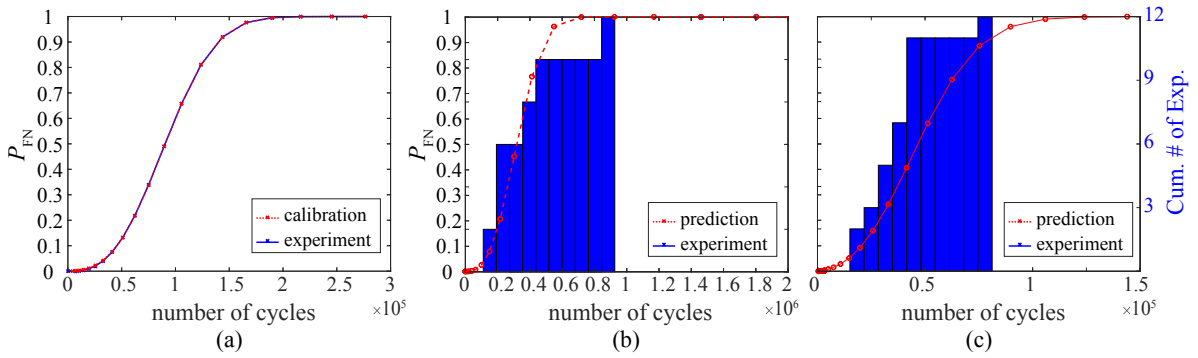

Figure 9: Probability of fatigue nucleation P_{FN} as a function of load cycles: (a) calibration at 91.5% of yield stress; (b) prediction at 85.8% of yield stress and (c) prediction at 95.5% of yield stress.

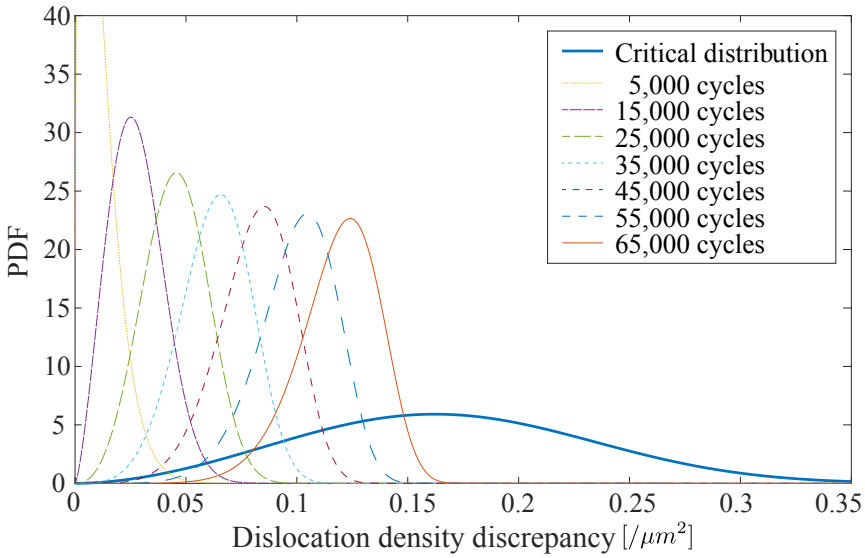

Figure 10: Distribution of D^3 and critical D^3.

loading) across the narrow load amplitude range, and this variation is very well captured by the model predictions. One of the primary reasons for the discrepancy between the predicted results and the model observations is that the number of experimental data points employed to generate the experimental probabilities of fatigue nucleation is relatively low as shown in Fig. 3.

6 Conclusion

This manuscript established a computational framework to predict fracture nucleation in polycrystalline microstructures under cyclic loading conditions. The proposed framework is probabilistic and considers the existence of an inherent property in the microstructure, i.e., a critical distribution of fatigue resistance that reflects the uncertainty induced by features that remain

unresolved at the scale of the grains. In view of the results of the proposed investigations, we make the following observations and conclusions: (1) A large ensemble of SVEs, of approximately an order of magnitude larger than what most previous studies considered is necessary to resolve the extreme value statistics at the microstructural scale. This observation emphasizes the need to employ fast solution algorithms in space and in time (e.g., reduced order models, machine learning models, time acceleration schemes) that allow for response evaluation of such large ensembles of SVEs over large number of cycles. (2) Validation of a probabilistic computational framework such as the one proposed requires a large experimental dataset, since extreme value statistics drive the nucleation process. To the best of our knowledge, there is no such dataset available in the open literature. (3) Furthermore, a thorough validation of model predictions would need direct (and sufficient number of) experimental observations of where and when fatigue cracks nucleate. In view of the large variability of number of cycles that nucleate fatigue cracks and the role of the microstructural features in nucleating those cracks, the proposed probabilistic computational framework offers a pathway for robust assessment of fatigue life in polycrystalline materials.

Acknowledgments

The authors gratefully acknowledge the financial support from the National Aeronautics and Space Administration, Space Technology Research Grants (Early State Innovation Grant No.: 80NSSC20K0294).

References

[1] W. Abuzaid, H. Sehitoglu, and J. Lambros. Plastic strain localization and fatigue micro-crack formation in hastelloy x. *Materials Science and Engineering: A*, 561:507–519, 2013.

[2] M. Anahid and S. Ghosh. Homogenized constitutive and fatigue nucleation models from crystal plasticity fe simulations of ti alloys, part 2: Macroscopic probabilistic crack nucleation model. *International Journal of Plasticity*, 48:111–124, 2013.

[3] F. Appel, U. Lorenz, M. Oehring, U. Sparka, and R. J. M. S. Wagner. Thermally activated deformation mechanisms in micro-alloyed two-phase titanium amminide alloys. *Materials Science and Engineering: A*, 233(1-2):1–14, 1997.

[4] P. J. Ashton, T.-S. Jun, Z. Zhang, T. B. Britton, A. M. Harte, S. B. Leen, and F. P. Dunne. The effect of the beta phase on the micromechanical response of dual-phase titanium alloys. *International Journal of Fatigue*, 100:377–387, 2017.

[5] R. Bandyopadhyay and M. D. Sangid. A probabilistic fatigue framework to enable location-specific lifing for critical thermo-mechanical engineering applications. *Integrating Materials and Manufacturing Innovation*, 10(1):20–43, 2021.

[6] R. Bandyopadhyay, V. Prithivirajan, and M. D. Sangid. Uncertainty quantification in the mechanical response of crystal plasticity simulations. *Jom*, 71(8):2612–2624, 2019.

[7] R. Bandyopadhyay, V. Prithivirajan, A. D. Peralta, and M. D. Sangid. Microstructure-sensitive critical plastic strain energy density criterion for fatigue life prediction across various loading regimes. *Proceedings of the Royal Society A*, 476(2236):20190766, 2020.

[8] I. J. Beyerlein and C. N. Tomé. A dislocation-based constitutive law for pure zr including temperature effects. *International Journal of Plasticity*, 24(5):867–895, 2008.

[9] G. Biallas, M. Essert, and H. J. Maier. Influence of environment on fatigue mechanisms in high-temperature titanium alloy imi834. *International journal of fatigue*, 27(10-12): 1485–1493, 2005.

[10] F. E. Bock, R. C. Aydin, C. J. Cyron, N. Huber, S. R. Kalidindi, and B. Klusemann. A review of the application of machine learning and data mining approaches in continuum materials mechanics. *Frontiers in Materials*, 6:110, 2019.

[11] J. D. Carroll, W. Abuzaid, J. Lambros, and H. Sehitoglu. High resolution digital image correlation measurements of strain accumulation in fatigue crack growth. *International Journal of Fatigue*, 57:140–150, 2013.

[12] G. M. Castelluccio and D. L. McDowell. Microstructure and mesh sensitivities of mesoscale surrogate driving force measures for transgranular fatigue cracks in polycrystals. *Materials Science and Engineering: A*, 639:626–639, 2015.

[13] G. M. Castelluccio and D. L. McDowell. Microstructure-sensitive small fatigue crack growth assessment: Effect of strain ratio, multiaxial strain state, and geometric discontinuities. *International Journal of Fatigue*, 82:521–529, 2016.

[14] G. M. Castelluccio, W. D. Musinski, and D. L. McDowell. Recent developments in assessing microstructure-sensitive early stage fatigue of polycrystals. *Current Opinion in Solid State and Materials Science*, 18(4):180–187, 2014.

[15] P. C. Collins, B. Welk, T. Searles, J. Tiley, J. C. Russ, and H. L. Fraser. Development of methods for the quantification of microstructural features in α+ β-processed α/β titanium alloys. *Materials Science and Engineering: A*, 508(1-2):174–182, 2009.

[16] R. Crouch and C. Oskay. Accelerated time integrator for multiple time scale homogenization. *International Journal for Numerical Methods in Engineering*, 101(13):1019–1042, 2015.

[17] R. Crouch, C. Oskay, and S. Clay. Multiple spatio-temporal scale modeling of composites subjected to cyclic loading. *Computational Mechanics*, 51(1):93–107, 2013.

[18] A. Cruzado, S. Lucarini, J. LLorca, and J. Segurado. Crystal plasticity simulation of the effect of grain size on the fatigue behavior of polycrystalline inconel 718. *International Journal of Fatigue*, 113:236–245, 2018.

[19] D. Deka, D. S. Joseph, S. Ghosh, and M. J. Mills. Crystal plasticity modeling of deformation and creep in polycrystalline ti-6242. *Metallurgical and materials transactions A*, 37(5):1371–1388, 2006.

[20] F. P. E. Dunne, A. J. Wilkinson, and R. Allen. Experimental and computational studies of low cycle fatigue crack nucleation in a polycrystal. *International Journal of Plasticity*, 23(2):273–295, 2007.

[21] S. Fujishiro and D. Eylon. Improvement of ti alloy fatigue properties by pt ion plating. *Metallurgical Transactions A*, 11(8):1259–1263, 1980.

[22] J. M. Garcia and T. F. Morgeneyer. Strength and fatigue strength of a similar ti-6al-2sn-4zr-2mo-0.1 si linear friction welded joint. *Fatigue & Fracture of Engineering Materials & Structures*, 42(5):1100–1117, 2019.

[23] N. Gey, M. Humbert, M. J. Philippe, and Y. Combres. Modeling the transformation texture of ti-64 sheets after rolling in the β-field. *Materials Science and Engineering: A*, 230(1-2):68–74, 1997.

[24] S. Ghosh, M. Mills, S. Rokhlin, V. Sinha, W. Soboyejo, and J. Williams. The evaluation of cold dwell fatigue in ti-6242. *US Dept. of Transportation/Federal Aviation Authority report, DOT/FAA/AR-06/24*, 2007.

[25] J. Gockel, N. Klingbeil, and S. Bontha. A closed-form solution for the effect of free edges on melt pool geometry and solidification microstructure in additive manufacturing of thin-wall geometries. *Metallurgical and Materials Transactions B*, 47(2):1400–1408, 2016.

[26] T. Gu, K. S. Stopka, C. Xu, and D. L. McDowell. Prediction of maximum fatigue indicator parameters for duplex ti–6al–4v using extreme value theory. *Acta Materialia*, 188:504–516, 2020.

[27] H. S. Ho, M. Risbet, X. Feaugas, and G. Moulin. The effect of grain size on the localization of plastic deformation in shear bands. *Scripta Materialia*, 65(11):998–1001, 2011.

[28] N. Hrabe, T. Gnäupel-Herold, and T. Quinn. Fatigue properties of a titanium alloy (ti–6al–4v) fabricated via electron beam melting (ebm): Effects of internal defects and residual stress. *International Journal of Fatigue*, 94:202–210, 2017.

[29] J. Jiang, J. Yang, T. Zhang, F. P. E. Dunne, and T. B. Britton. On the mechanistic basis of fatigue crack nucleation in ni superalloy containing inclusions using high resolution electron backscatter diffraction. *Acta Materialia*, 97:367–379, 2015.

[30] T. S. Jun, D. E. J. Armstrong, and T. B. Britton. A nanoindentation investigation of local strain rate sensitivity in dual-phase ti alloys. *Journal of Alloys and Compounds*, 672:282–291, 2016.

[31] T.-S. Jun, G. Sernicola, F. P. Dunne, and T. B. Britton. Local deformation mechanisms of two-phase ti alloy. *Materials Science and Engineering: A*, 649:39–47, 2016.

[32] M. E. Kassner, Y. Kosaka, and J. S. Hall. Low-cycle dwell-time fatigue in ti-6242. *Metallurgical and Materials Transactions A*, 30(9):2383–2389, 1999.

[33] K. Kitayama, C. N. Tomé, E. F. Rauch, J. J. Gracio, and F. Barlat. A crystallographic dislocation model for describing hardening of polycrystals during strain path changes. application to low carbon steels. *International Journal of Plasticity*, 46:54–69, 2013.

[34] S. Kotha, D. Ozturk, and S. Ghosh. Uncertainty-quantified parametrically homogenized constitutive models (uq-phcms) for dual-phase α/β titanium alloys. *npj Computational Materials*, 6(1):1–20, 2020.

[35] J. M. Larsen, S. K. Jha, C. J. Szczepanski, M. J. Caton, R. John, A. H. Rosenberger, D. J. Buchanan, P. J. Golden, and J. R. Jira. Reducing uncertainty in fatigue life limits of turbine engine alloys. *International journal of fatigue*, 57:103–112, 2013.

[36] P. Lefranc, C. Sarrazin-Baudoux, and V. Doquet. Dwell-fatigue behaviour of a beta-forged ti 6242 alloy. In *Fracture of Nano and Engineering Materials and Structures*, pages 171–172. Springer, 2006.

[37] C. Leyens and M. Peters. *Titanium and titanium alloys: fundamentals and applications*. John Wiley & Sons, 2003.

[38] D.-F. Li, R. A. Barrett, P. E. O'Donoghue, C. J. Hyde, N. P. O'Dowd, and S. B. Leen. Micromechanical finite element modelling of thermo-mechanical fatigue for p91 steels. *International Journal of Fatigue*, 87:192–202, 2016.

[39] Y. Liu, Y. Zhu, C. Oskay, P. Hu, L. Ying, and D. Wang. Experimental and computational study of microstructural effect on ductile fracture of hot-forming materials. *Materials Science and Engineering: A*, 724:298–323, 2018.

[40] Y. Liu, X. Zhang, Y. Zhu, P. Hu, and C. Oskay. Dislocation density informed eigenstrain based reduced order homogenization modeling: Verification and application on a titanium alloy structure subjected to cyclic loading. *Modelling and Simulation in Materials Science and Engineering*, 28(2):025004, 2020.

[41] G. E. R. D. Lütjering. Influence of processing on microstructure and mechanical properties of (α+ β) titanium alloys. *Materials Science and Engineering: A*, 243(1-2):32–45, 1998.

[42] R. Madec, B. Devincre, and L. P. Kubin. From dislocation junctions to forest hardening. *Physical review letters*, 89(25):255508, 2002.

[43] S. Mahadevan and A. Haldar. Probability, reliability and statistical method in engineering design. *John Wiley & Sons*, 2000.

[44] P. O. Maruschak, M. G. Chausov, I. V. Konovalenko, O. P. Yasnii, S. V. Panin, and I. V. Vlasov. Effect of shock and vibration loading on the fracture mechanisms of a vt23 titanium alloy. *Strength of Materials*, 52(2):252–261, 2020.

[45] F. McBagonluri, E. Akpan, C. Mercer, W. Shen, and W. O. Soboyejo. An investigation of the effects of microstructure on dwell fatigue crack growth in ti-6242. *Materials Science and Engineering: A*, 405(1-2):111–134, 2005.

[46] D. L. McDowell and F. P. E. Dunne. Microstructure-sensitive computational modeling of fatigue crack formation. *International journal of fatigue*, 32(9):1521–1542, 2010.

[47] H. Mecking and U. F. Kocks. Kinetics of flow and strain-hardening. *Acta metallurgica*, 29(11):1865–1875, 1981.

[48] J. Miao, T. M. Pollock, and J. W. Jones. Microstructural extremes and the transition from fatigue crack initiation to small crack growth in a polycrystalline nickel-base superalloy. *Acta Materialia*, 60(6-7):2840–2854, 2012.

[49] Mechanical Properties Data Center Traverse City Mich. *Aerospace Structural Metals Handbook. Volume III.* Defense Technical Information Center, 1972. URL `https://books.google.com/books?id=Y45vSwAACAAJ`.

[50] S. Naka, A. Lasalmonie, P. Costa, and L. P. Kubin. The low-temperature plastic deformation of α-titanium and the core structure of a-type screw dislocations. *Philosophical Magazine A*, 57(5):717–740, 1988.

[51] G. M. Owolabi, R. Prasannavenkatesan, and D. L. McDowell. Probabilistic framework for a microstructure-sensitive fatigue notch factor. *International Journal of Fatigue*, 32 (8):1378–1388, 2010.

[52] D. Ozturk, S. Kotha, and S. Ghosh. An uncertainty quantification framework for multi-scale parametrically homogenized constitutive models (phcms) of polycrystalline ti alloys. *Journal of the Mechanics and Physics of Solids*, 148:104294, 2021.

[53] V. T. Phan, X. Zhang, Y. Li, and C. Oskay. Microscale modeling of creep deformation and rupture in nickel-based superalloy IN 617 at high temperature. *Mech. Mater.*, 114: 215–227, 2017.

[54] A. L. Pilchak, W. J. Porter, and R. John. Room temperature fracture processes of a near-α titanium alloy following elevated temperature exposure. *Journal of Materials Science*, 47(20):7235–7253, 2012.

[55] C. P. Przybyla and D. L. McDowell. Microstructure-sensitive extreme value probabilities for high cycle fatigue of ni-base superalloy in100. *International Journal of Plasticity*, 26 (3):372–394, 2010.

[56] C. P. Przybyla and D. L. McDowell. Simulated microstructure-sensitive extreme value probabilities for high cycle fatigue of duplex ti–6al–4v. *International Journal of Plasticity*, 27(12):1871–1895, 2011.

[57] J. K. Qiu, Y. J. Ma, J. F. Lei, Y. Y. Liu, A. J. Huang, D. Rugg, and R. Yang. A comparative study on dwell fatigue of ti-6al-2sn-4zr-xmo (x= 2 to 6) alloys on a microstructure-normalized basis. *Metallurgical and Materials Transactions A*, 45(13):6075–6087, 2014.

[58] R. Quey, P. R. Dawson, and F. Barbe. Large-scale 3d random polycrystals for the finite element method: Generation, meshing and remeshing. *Computer Methods in Applied Mechanics and Engineering*, 200(17-20):1729–1745, 2011.

[59] M. D. Sangid, H. J. Maier, and H. Sehitoglu. An energy-based microstructure model to account for fatigue scatter in polycrystals. *Journal of the Mechanics and Physics of Solids*, 59(3):595–609, 2011.

[60] F. Sansoz and H. Ghonem. Effects of loading frequency on fatigue crack growth mechanisms in α/β ti microstructure with large colony size. *Materials Science and Engineering: A*, 356(1-2):81–92, 2003.

[61] S.Forest. Some links between cosserat, strain gradient crystal plasticity and the statistical theory of dislocations. *Philosophical Magazine*, 88(30-32):3549–3563, 2008.

[62] W. Shen, W. O. Soboyejo, and A. B. O. Soboyejo. An investigation on fatigue and dwell-fatigue crack growth in ti–6al–2sn–4zr–2mo–0.1 si. *Mechanics of materials*, 36(1-2): 117–140, 2004.

[63] J. Sieniawski, W. Ziaja, K. Kubiak, and M. Motyka. Microstructure and mechanical properties of high strength two-phase titanium alloys. *Titanium Alloys-Advances in Properties Control*, pages 69–80, 2013.

[64] V. Sinha, M. J. Mills, and J. C. Williams. Understanding the contributions of normal-fatigue and static loading to the dwell fatigue in a near-alpha titanium alloy. *Metallurgical and Materials Transactions A*, 35(10):3141–3148, 2004.

[65] V. Tong, S. Joseph, A. K. Ackerman, D. Dye, and T. B. Britton. Using transmission kikuchi diffraction to characterise α variants in an $\alpha+$ β titanium alloy. *Journal of microscopy*, 267(3):318–329, 2017.

[66] M. A. Tschopp, B. B. Bartha, W. J. Porter, P. T. Murray, and S. B. Fairchild. Microstructure-dependent local strain behavior in polycrystals through in-situ scanning electron microscope tensile experiments. *Metallurgical and Materials Transactions A*, 40 (10):2363–2368, 2009.

[67] B. Viguier, K. J. Hemker, J. Bonneville, F. Louchet, and J.-L. Martin. Modelling the flow stress anomaly in γ-tial i. experimental observations of dislocation mechanisms. *Philosophical Magazine A*, 71(6):1295–1312, 1995.

[68] S. Waheed, Z. Zheng, D. S. Balint, and P. E. Dunne. Microstructural effects on strain rate and dwell sensitivity in dual-phase titanium alloys. *Acta Materialia*, 162:136–148, 2019.

[69] X. G. Wang, V. Crupi, C. Jiang, and E. Guglielmino. Quantitative thermographic methodology for fatigue life assessment in a multiscale energy dissipation framework. *International journal of fatigue*, 81:249–256, 2015.

[70] G. Whelan and D. L. McDowell. Uncertainty quantification in icme workflows for fatigue critical computational modeling. *Engineering Fracture Mechanics*, 220:106673, 2019.

[71] G. Whelan and D. L. McDowell. Machine learning-enabled uncertainty quantification for modeling structure–property linkages for fatigue critical engineering alloys using an icme workflow. *Integrating Materials and Manufacturing Innovation*, 9(4):376–393, 2020.

[72] D. Wilson and F. P. E. Dunne. A mechanistic modelling methodology for microstructure-sensitive fatigue crack growth. *Journal of the Mechanics and Physics of Solids*, 124: 827–848, 2019.

[73] M. Yaghoobi, K. S. Stopka, A. Lakshmanan, V. Sundararaghavan, J. E. Allison, and D. L. McDowell. Prisms-fatigue computational framework for fatigue analysis in polycrystalline metals and alloys. *npj Computational Materials*, 7(1):1–12, 2021.

[74] S. R. Yeratapally, M. G. Glavicic, M. Hardy, and M. D. Sangid. Microstructure based fatigue life prediction framework for polycrystalline nickel-base superalloys with emphasis on the role played by twin boundaries in crack initiation. *Acta Materialia*, 107:152–167, 2016.

[75] S. R. Yeratapally, M. G. Glavicic, C. Argyrakis, and M. D. Sangid. Bayesian uncertainty quantification and propagation for validation of a microstructure sensitive model for prediction of fatigue crack initiation. *Reliability Engineering & System Safety*, 164:110–123, 2017.

[76] F. Yuan, C. Liu, H. Gu, F. Han, Y. Zhang, M. Ali, and G. Li. Effects of mechanical polishing treatments on high cycle fatigue behavior of ti-6al-2sn-4zr-2mo alloy. *International Journal of Fatigue*, 121:55–62, 2019.

[77] M. Zecevic and M. Knezevic. A dislocation density based elasto-plastic self-consistent model for the prediction of cyclic deformation: Application to aa6022-t4. *International Journal of Plasticity*, 72:200–217, 2015.

[78] X. Zhang and C. Oskay. Eigenstrain based reduced order homogenization for polycrystalline materials. *Computer Methods in Applied Mechanics and Engineering*, 297:408–436, 2015.

[79] X. Zhang and C. Oskay. Sparse and scalable eigenstrain-based reduced order homogenization models for polycrystal plasticity. *Computer Methods in Applied Mechanics and Engineering*, 326:241–269, 2017.

[80] X. Zhang and C. Oskay. Material and morphology parameter sensitivity analysis in particulate composite materials. *Computational Mechanics*, 62(3):543–561, 2018.

[81] X. Zhang and C. Oskay. Plastic dissipation sensitivity to mechanical properties in polycrystalline β-hmx subjected to impact loading. *Mechanics of Materials*, 138:103079, 2019.

[82] X. Zhang and C. Oskay. Modeling and numerical investigation of mechanical twinning in β-hmx crystals subjected to shock loading. *Modelling and Simulation in Materials Science and Engineering*, 29(7):075009, 2021.

[83] Z. Zhang and F. P. Dunne. Microstructural heterogeneity in rate-dependent plasticity of multiphase titanium alloys. *Journal of the Mechanics and Physics of Solids*, 103:199–220, 2017.

[84] Z. Zhang and F. P. Dunne. Phase morphology, variants and crystallography of alloy microstructures in cold dwell fatigue. *International Journal of Fatigue*, 113:324–334, 2018.